Organic Electronics 120 (2023) 106843

Contents lists available at ScienceDirect

Organic Electronics

journal homepage: www.elsevier.com/locate/orgel

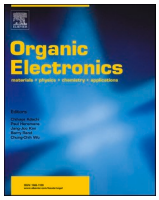

Temperature behaviour of mixed-cation mixed-halide perovskite solar cells. Analysis of recombination mechanisms and ion migration

Mari Carmen López-González [a,*], Gonzalo del Pozo [a], Belén Arredondo [a], Silvia Delgado [a], Diego Martín-Martín [a], Marina García-Pardo [b], Beatriz Romero [a]

[a] Electronic Technology Area, Universidad Rey Juan Carlos (DELFO-URJC), Móstoles, 28933, Madrid, Spain
[b] Instituto de Óptica, IO-CSIC (Laser Processing Group), 28006, Madrid, Spain

ARTICLE INFO

Keywords:
Perovskite
Ion migration
Carrier recombination
Mixed-cation mixed-halide

ABSTRACT

In our study, we show that compositional engineering of the "A" site cation of ABX_3 perovskite structure formed by a mix of organic and inorganic cations is an effective route to improve the thermal stability of perovskite solar cells (PSCs). In this work, mixed-cation mixed-halide PSCs have been fabricated and characterized with temperature, from 253 up to 333 K. The active layer based on $CsRbFAMAPb(IBr)_3$ results in a more stable device compared to standard $MAPbI_3$ devices. Electrical characterization reveals a decrease of the solar cell parameters with temperature. Using Impedance Spectroscopy (*IS*) characterization, we have estimated an activation energy for the halide ion migration of 0.63 ± 0.08 eV, an ion diffusion coefficient of 10^{-14} $cm^2\,s^{-1}$, and a defect density of $7.27{\cdot}10^{15}$ cm^{-3}. To our knowledge, this is the first time that these parameters have been calculated in $CsRbFAMAPb(IBr)_3$ based devices, resulting in improved values compared to $MAPbI_3$ devices. The worsening of device performance for temperatures above 300 K is attributed to a decrease of the spiro-OMeTAD conductivity and the degradation of the perovskite/spiro-OMeTAD interface. It is shown that for low temperatures (from 253 to 323 K), Shockley-Red-Hall (SRH) recombination in the bulk governs, while for temperatures above 323 K the increase in surface recombination becomes dominant due to the presence of non-selective contacts.

Numerical simulations using SILVACO ATLAS corroborate the role of SRH in the perovskite active layer for low and medium temperatures, and the crucial influence of spiro-OMeTAD transport properties in the device performance parameters.

1. Introduction

Since 2009 [1], PSCs have experienced a significant increase in their performance, making them one of the most promising technologies for use in both terrestrial and space applications [2]. Currently, the power conversion efficiency (PCE) record is set to 25.7%, competing with crystalline silicon, cadmium telluride and other stablished high-performance solar cells [3]. The reasons for this success are found in their excellent optoelectronic properties such as tuneable direct bandgap [4], high absorption coefficient [5], high carrier mobilities [6], long diffusion lengths [7], and high defect tolerance [8,9]. Moreover, their lightness, semitransparency, flexibility, and low-cost fabrication techniques are additional features that make PSCs a potential attractive and sustainable alternative to traditional silicon solar cells [10]. However, despite the great progress in device performance, the stability of PSCs remains a key factor for the ultimate success of commercial applications [11–13]. It is well known that exposure to moisture [14], oxygen [15–17], UV light [17–20], radiation [21], and elevated temperatures [22–24] results in a significant performance and/or durability decrease [25].

For terrestrial applications, solar cells suffer substantial temperature variations during day and night as well as during winter and summer or geographical position, which can influence the properties of the materials employed in an electronic device [26]. For outdoor terrestrial photovoltaic applications, the typical operating temperature range is approximately −20 °C to 85 °C [27]. To date, apart from widely adopted characterizations at room-temperature (RT), temperature dependent studies of PSCs have been very scarce [28–31]. Furthermore, it is important to note that there have been substantial advances regarding material synthesis and device engineering, but there are not many studies focused on characterizing the solar cell performance as function of temperature [2].

* Corresponding author.
E-mail address: mcarmen.lopez@urjc.es (M.C. López-González).

https://doi.org/10.1016/j.orgel.2023.106843
Received 8 March 2023; Received in revised form 26 April 2023; Accepted 30 April 2023
Available online 5 May 2023

Improved device stability is directly related to ABX_3 perovskite structures, where A and B are cations, with A being of larger size than B, and X is an anion [32]. As an ionic material, perovskite has low formation and migration activation energies of ionic species. For this reason, a large number of ions are mobile in the presence of an applied voltage. Mobiles ions can migrate towards and into the adjacent contact layers, resulting in a degradation of their charge extracting/transporting functionality with significant negative consequences on the long-term stability of PSCs [33]. Many different options have been studied to improve the stability of PSCs, both alone and combining different cations in the so-called mixed-cation perovskites. The most common A cations are organic methyl-ammonium ($CH_3NH_3^+$, MA^+), formamidinium ($CH_2(NH_2)_2^+$, FA^+), or inorganic rubidium (Rb^+) or cesium (Cs^+). The B site is occupied by a divalent inorganic cation, with lead (Pb^{2+}) being the most common choice. Finally, X is a halide anion such as iodine (I^-), bromine (Br^-), chorine (Cl^-) or fluorine (F^-) [34,35]. Pure $MAPbX_3$ and $FAPbX_3$ perovskites degrade easily mainly due to thermal or structural instabilities [36–39]. The partial substitution of MA^+ by FA^+ significantly enhances the performance and stability of perovskite material. However, even for these double cation perovskites, the presence of detrimental, photoinactive δ phase ("yellow phase", non-perovskite phase) impurities remains being the main cause of long-term instability. To date, compositional engineering of both cation and halide has been used to improve the structural and thermal stability of perovskites [40]. In general, increasing the perovskite complexity by adding more inorganic elements raises the entropy of the mix, and it can improve the morphology of the perovskite films. The undesirable δ and PbI_2 phases are transformed into α phase ("black phase", perovskite phase), and the formation of impurities is avoided [41,42]. Several research groups have worked on the addition of small amounts of inorganic cations (Cs^+ and Rb^+) with the aim of improving thermal stability. This resulted in an improved perovskite morphology with larger grains and smaller surface roughness [34,40–45]. Saliba et al. showed that mixing organic cation such as MA^+ or FA^+ with small amounts of Cs^+ or Rb^+ cations can facilitate the stabilization of the photoactive perovskite phase over a wide temperature range, resulting in stable devices at 85 °C for 500 h under continuous illumination and maximum power tracking [41]. Hu et al. demonstrated that the incorporation of Cs^+ significantly reduces the number and depth of traps which boost both the fill factor (*FF*) and the open circuit voltage (V_{OC}), as well as decreases the second-order recombination rate of free mobile charges in the active layer. On the other hand, Rb^+-addition reduces current-voltage hysteresis and increases carrier mobility [45].

Regardless the device architecture, PSCs are constituted by different layers, both organic and inorganic (multilayer structure). Therefore, the temperature dependence of a PSC performance can be influenced not only by the behaviour of the perovskite active layer, but also by the buffer layers and interfaces. For example, the thermal degradation associated with the most common material for the Hole Transport Layer (HTL), 2,2′,7,7′-tetrakis[N,N-di(4-methoxyphenyl)amino]-9,9′-spirobifluorene (spiro-OMeTAD), is related to the additives used to enhance its electrical conductivity. Glass transition temperature (T_g) of pure spiro-OMeTAD layer is 124 °C, but the cosolvent 4-tert-butylpyridine (tBP), which is added to increase the solubility of the dopant bis(trifluoromethylsulfonyl)imide lithium salt (Li-TFSI), reduces the T_g of spiro-OMeTAD to 72 °C [46]. Furthermore, the LiTFSI dopants are highly hygroscopic. Therefore, the performance of these devices can be reduced even at temperatures of 50 °C due to changes in the transport properties of the spiro-OMeTAD [47–49]. On the other hand, Domanski et al. have shown that exposing PSCs to 70 °C is enough to induce gold migration from the top electrode through the spiro-OMeTAD layer into the perovskite layer [50]. One alternative to spiro-OMeTAD is the polymer poly[bis(4-phenyl)-(2,4,6-trimethylphenyl)amine] (PTAA) with a T_g (94 °C) lower than that of spiro-OMeTAD. However, PTAA requires a smaller amount of Li-TFSI and therefore less tBP is needed [46].

Despite the remarkable progress that has been made in material and layer structure engineering, previous studies of thermal induced degradation are still very limited. Therefore, understanding the temperature behaviour of PSCs and how it affects the recombination processes is essential to fully comprehend the physical mechanisms taking place in these devices, and to provide a direction to develop effective strategies to further improve their performance and stability.

In this work, we have fabricated mixed-cation mixed-halide PSCs based on $(Cs_{0.05}Rb_{0.05}(FA_{0.83}MA_{0.17})_{0.9}Pb(I_{0.83}Br_{0.17})_3$, hereinafter referred to as CsRbFAMA, in a n-i-p solar cell with mesoscopic structure FTO/*c*-TiO_x/*m*-TiO_x/perovskite/spiro-OMeTAD/Au and analysed the temperature dependence performance. We have measured the current density-voltage (*J-V*) and obtained the temperature dependence of the solar cell parameters from 253 K up to 333 K. Moreover, we have characterized the cells using *IS* and the Cole-Cole spectra have been fitted using the Matryoshka circuit. We have quantified, for the first time, the activation energy for the halide ion migration, ion diffusion coefficient and the defect density in CsRbFAMA using Mott Schottky analysis. This quantification provides a better understanding of ion migration, which is essential for the stability of perovskite solar cells.

In addition, 2D numerical simulation using SILVACO ATLAS TCAD were performed for different illumination intensities, as a function of temperature. Electron, hole, and ion densities were calculated using the drift-diffusion transport model and solving the carrier/ion continuity equations, which includes trap-assisted (SRH), radiative recombination within the perovskite active layer, and surface recombination in the perovskite/HTL interface. Results have shown that device behaviour is dominated by SRH recombination at low temperature, in good agreement with experimental trends.

In summary, this paper contributes to improve the understanding of, on one hand, the high stable configuration of quadruple cation mixed halide perovskite solar cells, and, on the other hand, the dominant recombination process and the effect of temperature on the device performance.

2. Experimental methods

2.1. Device fabrication

Solar cells were fabricated on fluorine-doped tin oxide (FTO) coated glass substrates with a sheet resistance of 12–14 Ω/square. Prior to fabrication, patterned glass/FTO substrates were brushed with 2% Hellmanex water solution and rinsed with deionized water. After that, they were sequentially cleaned in consecutive ultrasonic baths for 15 min with Hellmanex solution, deionized water, isopropanol, and acetone, followed by UV-ozone treatment for 15 min. Next, a compact layer of TiO_2 (*c*-TiO_2) was deposited on FTO via spray pyrolysis at 450 °C from a precursor solution of titanium diisopropoxide bis(acetylacetonate) in absolute ethanol using oxygen as carrier gas. After the spraying, the substrates were kept at 450 °C for 30 min and cooled down to RT. The mesoporous solution (*m*-TiO_2) was prepared using a commercial TiO_2 paste (Sigma-Aldrich, 18NRT) diluted in absolute ethanol and deposited on *c*-TiO_2 samples by spin coating 100 μL for 10 s at 4000 rpm with a ramp speed of 2000 rpm/s. After spin coating, the substrates were immediately dried at 125 °C for 10 min and then heated following a temperature ramp up to 450 °C. Both *c*-TiO_2 and *m*-TiO_2 form the Electron Transport Layer (ETL). To deposit the remaining layers, the samples were transferred to a nitrogen glovebox (O_2 and H_2O levels below 1 ppm). The perovskite films were deposited from a precursor solution containing $FAPbI_2$ and $MAPbBr_2$ both in 4:1 %V DMF:DMSO (N,N-dimethylformamide:dimethyl sulphoxide) to which 5 %V of CsI solution in DMSO and 5 %V of RbI solution in 4:1 %V DMF:DMSO were added. The perovskite solution was spin coated in a two-step method: 1) 1000 and 6000 rpm for 10 and 20 s, respectively. During the second step, 200 μL of chlorobenzene were added as antisolvent on the spinning substrate 5 s before the sample stopped. The substrates were then

annealed on a hot plate at 100 °C for 60 min. To deposit the HTL a spiro-OMeTAD (Ossila) solution in chlorobenzene was used. The solution was doped with Li-TFSI, tris(2-(1H-pyrazol-1-yl)-4-tert-butylpyridine)-cobalt(III) tris(bis(trifluoromethylsulfonyl)imide) (FK209) and tBP, with molar ratio of 0.5, 0.03 and 3.3, respectively. Finally, a layer of gold (Au) deposited by thermal evaporation under high vacuum was used as top electrode.

The layer structure is shown in Fig. 1.

2.2. Device characterization

Electrical measurements were carried out using an Autolab potentiostat/galvanostat model PGSTAT204 (Eco-Chemie), equipped with the FRA32 M impedance module and the Metrohm Autolab optical bench. The instrument was controlled by the NOVA 2.1.4 software. *J-V* characteristics were performed under 1000 W m^{-2} illumination (equivalent to 1-sun) with an AM1.5G spectrum using an LED-based Solar Simulator (model Newport Oriel Verasol-2 class AAA). Device area is 0.3 cm^2, and they were characterized using a 0.13 cm^2 shadow mask.

Reverse and forward *J-V* curves recorded using a voltage scan rate of 20 mV/s showed no hysteresis behaviour. For this reason, the characteristic parameters (V_{OC}, short-circuit current density, J_{SC}, *FF* and PCE) have been extracted from *J-V* curves measured in reverse direction (from V_{OC} to J_{SC}) using this scan rate.

Temperature-dependent solar cell characterization was performed in nitrogen (N_2) atmosphere (to avoid condensed water at low temperatures), transferring the sample into a customized-built chamber. Due to absorption and reflection losses of the double quartz window, there was a drop in light intensity that reaches the sample from 1-sun to approximately 0.85 suns. The temperature was controlled using a Peltier plate placed at the base of the chamber and a INSTEC mK2000 temperature controller. All samples were first measured at RT (298 K), and next the temperature was swept from 253 K to the 333 K in 10 K or 20 K steps and finally back to RT.

J-V characterization in a broad range of light intensities (0.25, 0.5, 0.75 and 1-sun) was carried out using the solar simulator. To evaluate the dominant recombination mechanism in the device, the ideality factor (η) was extracted from these DC measurements. Furthermore, *IS* characterization was carried out in dark in a DC bias voltage range of 0–1 V and under 1-sun illumination at V_{OC} at different temperatures. Frequency ranged between 1 MHz and 0.1 Hz, applying sinusoidal signal of 20 mV amplitude. Experimental data were fitted using Scribner's ZView software. From these measurements, the activation energy for halide ion migration, diffusion coefficient, and defect density in the active layer were estimated.

2.3. Thin film characterization

Scanning electron spectroscopy (SEM) images were obtained using a high-resolution Nova Nano SEM230 microscope. Absorption spectra were acquired on a Cary 5000 UV–Vis–NIR spectrophotometer. The measurement was performed in transmission mode on a thin layer of perovskite. The measured active area corresponds with a spot with diameter of 1.6 cm. External Quantum Efficiency (EQE) was obtained using the LED-based Solar Simulator (model Newport Oriel Verasol-2 class AAA) which has 19 LEDs at different wavelengths from 420 to 1050 nm.

3. Results and discussion

Fig. 2 shows a cross-sectional SEM image of the device with a continuous and uniform *c*-TiO_2 layer of 45 nm, a *m*-TiO_2 layer of 180 nm with homogeneous nanoparticles as scaffolds filled with the active layer, and a 460 nm perovskite layer composed of large crystals without the presence of pinholes. A 190 nm layer of spiro-OMeTAD is deposited on top of the perovskite layer, and finally, a gold top electrode of around 70–90 nm is thermally evaporated to contact the device. The glass substrate with a 400–450 nm layer of FTO conforms the frontal contact. The PCE of our champion device with this architecture is 15.54%.

The average solar cell parameters of the 32 measured cells, at room temperature, are $V_{OC} = 1.08 \pm 0.03$ V, a $J_{SC} = 17.41 \pm 0.59$ mA/cm^2, a $FF = 0.75 \pm 0.03$, and a PCE = 14.1 ± 0.9%. Fig. 3 shows the parameters and the *J-V* curve of the champion device, measured at AM1.5G.

CsRbFAMA-based solar cells are temperature sensitive, as other photovoltaic technologies. Fig. 4 summarizes the temperature dependence of the solar cell parameters. As it was previously mentioned, due to absorption and reflection losses from the double quartz window of the temperature chamber, there was a drop in intensity of the incident light onto the solar cell. For this reason, in the temperature measurements, the PCE value is underestimated.

Overall, in the temperature range of 253 K–333 K, the PCE drops due to a reduction in V_{OC}, J_{SC} and *FF*. Looking closely, the PCE remains almost unaffected up to 300 K, varying from 12.4% to 11.6%, and then it decreases down to 8.4% when the temperature increases up to 333 K. The reasons for the decrease in the power conversion efficiency will be analysed in the following sections.

The physical interpretation of V_{OC} can be expressed as a result of the balance between generation and recombination of carriers, since no net current flows through the external contacts. V_{OC} is the most sensitive parameter to temperature variations in PSCs. The decrease of V_{OC} is linear with increasing temperature, leading to a negative temperature coefficient as occurs in other solar cell technologies [51]. According to Dupré et al., the temperature coefficient correlates the decrease in V_{OC} when temperature increases, and it can be approximated by the

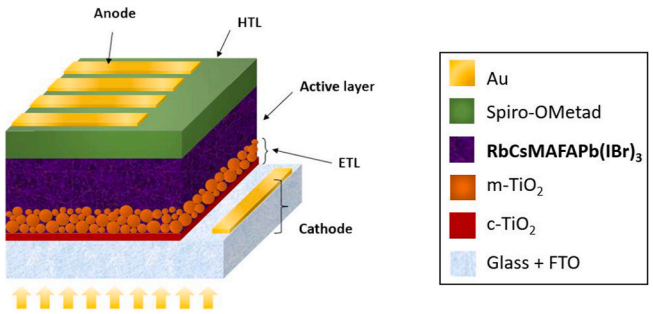

Fig. 1. Schematic representation of the device architecture of the PSCs.

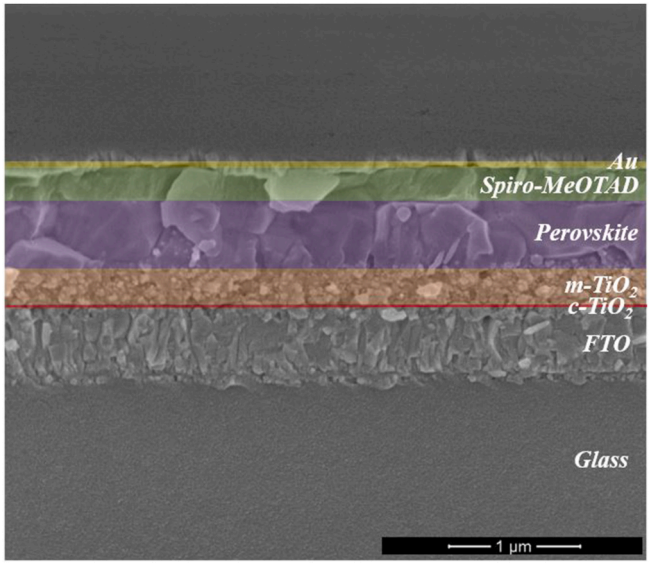

Fig. 2. Cross-sectional SEM image of the device.

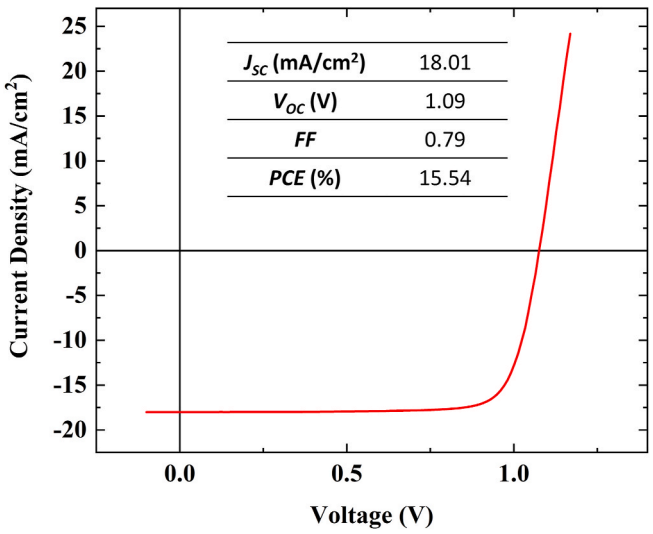

Fig. 3. *J-V* curve and parameters of the best performing device.

following simple linear relation [52]:

$$\beta_{V_{OC}}(T_C) = \frac{10^6}{V_{OC}(25\,^\circ C)} \frac{V_{OC}(T_C) - V_{OC}(25\,^\circ C)}{T_C - 25\,^\circ C} \quad (1)$$

where β_{Voc} is the temperature coefficient in parts per million (ppm)/°C and T_C is the temperature of the solar cell. The best way to understand the general dependences of V_{OC} with temperature is to make use of the p-n junction equations:

$$n_i = \sqrt{N_D N_A} e^{-E_g/2k_B T} \quad (2)$$

$$J_0 = n_i^2 qA \left(\frac{1}{N_D} \sqrt{\frac{D_p}{\tau_p}} + \frac{1}{N_A} \sqrt{\frac{D_n}{\tau_n}} \right) \quad (3)$$

$$V_{OC} = \frac{\eta k_B T}{q} ln\left(\frac{J_{SC}}{J_0} + 1 \right) \quad (4)$$

where n_i is the intrinsic carrier concentration, N_D and N_A are donor and acceptor density of states, respectively, E_g is the bandgap, k_B is Boltzmann's constant, T is temperature, J_0 is the dark saturation current, q is elementary charge, A is area, D_p and D_n are hole and electron diffusion coefficients, respectively, τ_p and τ_n are hole and electron carrier lifetimes, respectively, and η is the ideality factor. With regard to these equations and according to Green et al., the decrease of V_{OC} with increasing temperature is predominantly due to a continuous increase in the dark saturation current [53]. It is well known that J_0 rises with temperature as a result of the increase of the intrinsic carrier concentration leading to larger rates of recombination.

To determine the dominant recombination pathways, the temperature dependence of V_{OC} is used to evaluate the activation energy (E_a) of the dominant recombination mechanism by extrapolating the data to $T = 0$ K. The extrapolated line intersects the V_{OC} axis at 1.49 eV (inset in Fig. 4.b), giving a value lower than the perovskite bandgap, set in $E_g =$

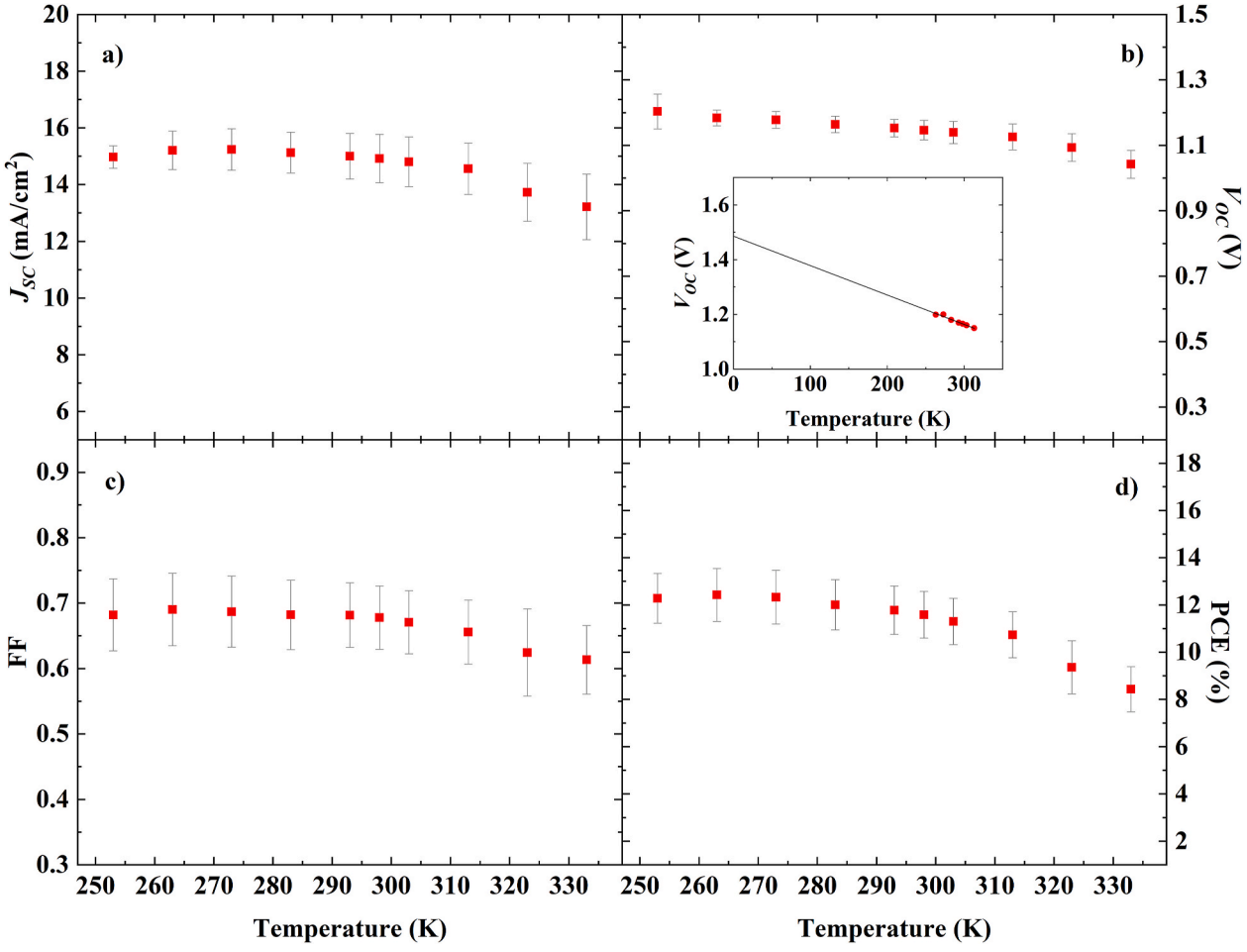

Fig. 4. Evolution of the solar cell parameters with temperature. The mean and the standard deviation are shown for a batch of 32 devices. Inset in Fig. 4b shows the extrapolation of V_{OC} at 0 K.

1.60 eV, which was extracted from the Tauc plot of absorption (Fig. 5). According to Tress et al., $E_a < E_g$ is commonly attributed to carrier recombination at heterojunction interfaces or surfaces. Moreover, tail states and non-selective contacts can lead to a reduced E_a [54].

To gain insight into the recombination mechanisms, the ideality factor is determined by evaluating the slope of the plot V_{OC} vs. logarithmic irradiation light intensity, ln(I_{light}), at different temperatures, see Fig. 6. The slope of V_{OC} with light intensity is constant and leads to a η ~1.5 and 1.2 for 263 K and 298 K respectively, suggesting that SRH governs the recombination [54], and indicating that as the temperature increases SRH recombination is governed by the interface. Furthermore, at even higher temperatures (above 323 K), V_{OC} saturates at high light intensity. This results in two different V_{OC} slopes that give rise to two different ideality factors, η ~1.2 in the low intensity region, and η < 1 at higher intensities. It is well known that V_{OC} is limited by the built-in potential (V_{bi}, defined as the difference of the electrodes work functions) and in the presence of non-selective contacts it saturates with light intensity as it approaches V_{bi}. According to Tress et al., in this scenario (η < 1 and non-selective contacts), surface recombination is the dominant recombination mechanism. A low ideality factor is not necessarily beneficial for the device performance and can lead to a lower V_{OC} compared to the case where η > 1 and V_{OC} is limited by SRH recombination in the bulk [54]. Thus, this decrease of the ideality factor below one at high temperatures is an indicative that thermal degradation is taken place at one device interface. This hypothesis will be further discussed.

Regarding J_{SC}, it is generally controlled by the band gap energy, the absorption coefficient, and the charge extraction efficiency. The underlying physical mechanisms explaining the decrease of J_{SC} with temperature in perovskite solar cells still remain unclear. An increase of E_g causes a reduction in the spectral absorption range, while the collected fraction of incident photons increases typically with temperature [55]. Therefore, the J_{SC} behaviour with temperature depends on which of these two mechanisms dominates. Temperature-dependent EQE spectra were recorded and E_g was extracted using an estimation of external radiative efficiency (ERE) proposed by Green [56]. As shown in Fig. 7, the change in EQE onsets leads to a shift in E_g, which slightly increases with temperature (inset in Fig. 7). This behaviour of E_g with temperature is opposite to inorganic semiconductors and it has been previously reported in literature [26,27,52,57]. However, the 11.7% decrease in J_{SC} cannot be explained solely by such a small increase in E_g. The observation that EQE barely changes with temperature, while J_{SC} decreases with it, is attributed to the fact that the measurements were performed at very

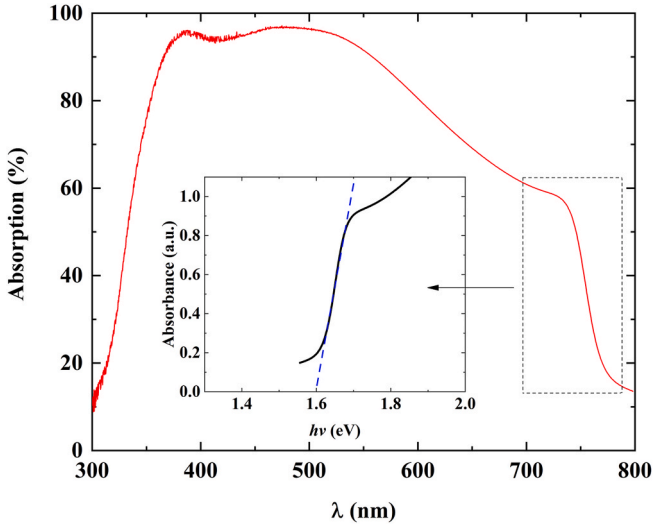

Fig. 5. Absorption spectrum at room temperature. Inset shows the Tauc plot and the extracted E_g.

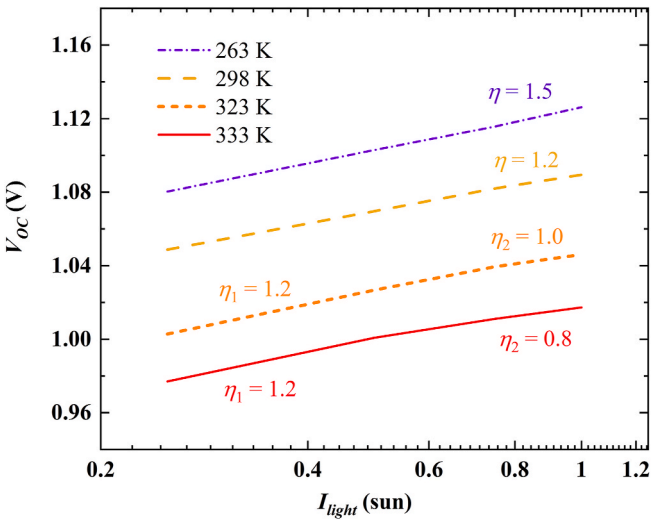

Fig. 6. V_{OC} as a function of illumination intensity for different temperatures.

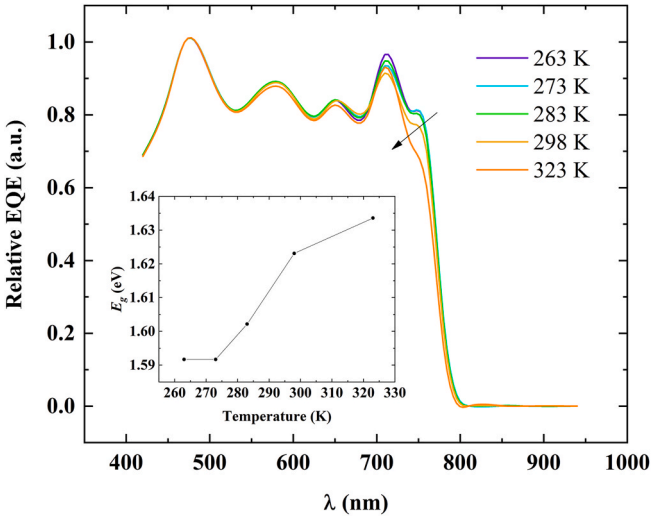

Fig. 7. Evolution of external quantum efficiency with temperature. Inset shows the calculated E_g with temperature obtained from the EQE.

different light intensities regimes. It is worth noticing that EQE was measured at low illumination levels, and therefore it is not limited by interface recombination. Therefore, we can infer that the change in J_{SC} is not governed by a decrease in the absorption properties of the perovskite, but more likely by recombination losses or inefficient charge extraction.

Fig. 4c shows a decrease of the FF with temperature which is commonly attributed to an increase of the overall device resistance (R_T). At high temperatures, the R_T increases, worsening the conductivity and strongly deteriorating the charge extraction. We suspect that this increase in R_T is due to a degradation of the spiro-OMeTAD layer with temperature. Previous studies reported that the conductivity and hole collection ability of spiro-OMeTAD decreases at high temperature [49,58]. According to Kim et al., at elevated temperatures the oxidation of spiro-OMeTAD is reduced and, consequently, so it is its electrical conductivity, due to the diffusion of the iodide ions from the perovskite. In addition, Jena et al. attributed the decrease in PSCs performance to morphological changes (generation of voids) caused by the crystallization and photo-oxidation of spiro-OMeTAD at high temperature, which in turn results in a decrease of the hole mobility. Therefore, as we will confirm later with impedance measurements, the worsening in

performance of these devices at high temperature is not attributed to the degradation of the perovskite layer CsRbFAMA itself, but it is likely due to the modification of the spiro-OMeTAD conduction ability and the deterioration of the perovskite/spiro-OMeTAD interface. It should be noted that, the absorption of active layer and spiro-OMeTAD layer does not change with temperature. This is in good agreement with the previous hypothesis of the surface recombination being the dominant recombination mechanism at high temperatures since the ETL synthesizes at 450 °C and it is not affected by experimental temperature changes.

In order to obtain a deeper insight into the dynamical mechanisms taking place in the device, samples were characterized using *IS* in a temperature range of 263–313 K. *IS* is a frequency characterization technique which allows decoupling physical responses with different characteristic times [59–62]. Fig. 8 shows the Nyquist plots obtained as a function of temperature at open circuit under 1-sun illumination. Two semi-circular features, that are typical for any PSC device [63–65], with two relaxation processes are clearly observed, at high and low frequency respectively. The high frequency semi-circle is usually attributed to charge recombination, while the one in the low-frequency region has been previously attributed to ionic diffusion and, eventually, ionic accumulation at the interfaces of the perovskite and the selective contact [66]. The Nyquist plot can be modelled with the circuit shown in the inset of Fig. 8, known as Matryoshka configuration [65]. The circuit is a combination of the external series resistance (R_S), two resistive elements (R_{HF}, R_{LF}) and two non-ideal capacitive elements named constant-phase element (CPE_{HF}, CPE_{LF}). The impedance of a CPE is given by $Z_{CPE} = 1/[Q(j\omega)^{\alpha}]$ [67], where Q is a parameter with units $F\cdot(Hz)^{(1-\alpha)}$. C_{HF} is an effective capacitance defined as $C_{HF} = (Q\cdot R_{HF})^{1/\alpha}\cdot R_{HF}^{-1}$ and represents the geometrical capacitance, associated with the dielectric constant of the perovskite layer. C_{LF}, defined as $C_{LF} = (Q\cdot R_{LF})^{1/\alpha}\cdot R_{LF}^{-1}$, has been related to ion diffusion and, eventually, ionic accumulation at the interfaces between the perovskite and the selective contact [66]. Moreover, the resistance R_S models ohmic contribution of the contacts and wires, R_{HF} is associated to carrier recombination, and R_{LF} has been previously associated with several processes such as carrier accumulation resistance at the interfaces, surface resistance, and slow processes, such as ion diffusion and trap-mediated charge recombination in the bulk [68–70].

Since one of the objectives of this work is to obtain information about the behaviour of ions, we have focused on the low frequency region. The circuital model fits the low frequency semicircle well enough, and the resulting parameters are shown in Fig. 9. As we can see, R_{LF} remains practically constant with increasing temperature while C_{LF} decreases. At high frequency, the fit could be improved with a more complex circuit.

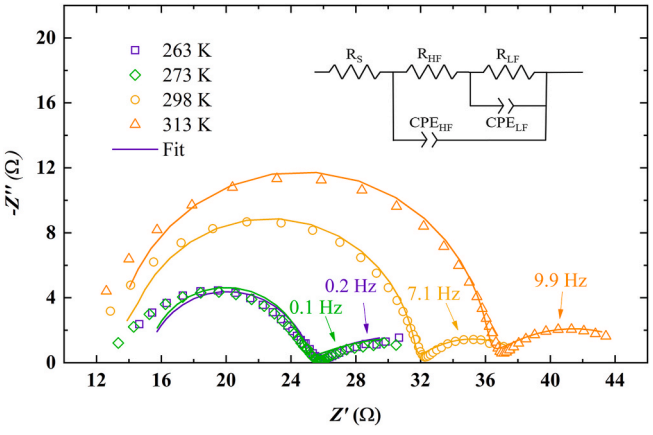

Fig. 8. Nyquist plot as a function of temperature. Experimental measurements (symbols), circuital fit (solid line). Equivalent circuital model used to fit experimental *IS*.

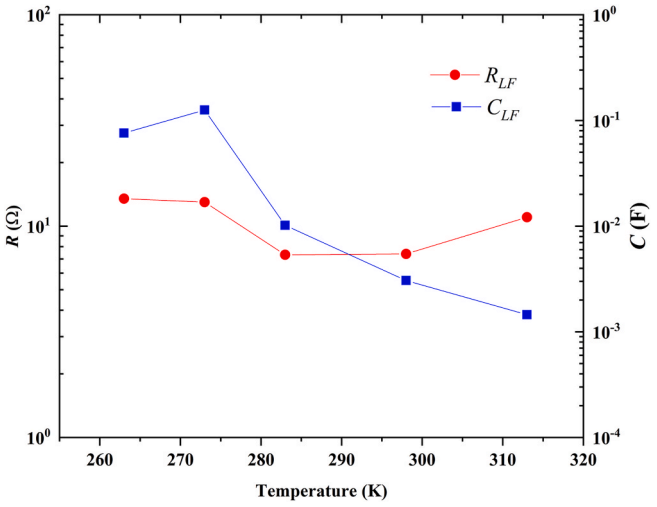

Fig. 9. Evolution with temperature of Low Frequency parameters extracted from *IS*.

Nevertheless, we can state that the extracted parameters would remain almost constant in this temperature range with values around $R_{HF} \approx 4\ \Omega\ cm^2$ and $C_{HF} \approx 322\ nF/cm^2$.

As the low frequency arc is associated to ion diffusion, we have used the temperature dependence of the low frequency time constant to estimate the activation energy of the halide ion migration. Fig. 10 shows the Arrhenius plot of the low frequency time constant, defined as $\tau_{LF} = R_{LF}\cdot C_{LF}$, obtained from the fit of the impedance spectra at different temperatures using the circuit of the inset in Fig. 8. The activation energy for ion migration (E_{ion}) is related to τ_{LF} and to the temperature by the following equation [71]:

$$\frac{1}{\tau_{LF}} = Be^{-\frac{E_{ion}}{k_B T}} + C \tag{5}$$

where B is the Arrhenius prefactor, k_B is the Boltzmann constant, T is the temperature, and C is a constant.

Using Eq. (5) we calculated an ion activation energy of $E_{ion} = 0.63 \pm 0.08$ eV for the iodide ions. It is widely accepted that iodide ions (I^-) are mobile in archetypal $MAPbI_3$. Previous works [72–76] indicate that $MAPbI_3$ is a mixed ionic-electronic conductor and iodide ion transport

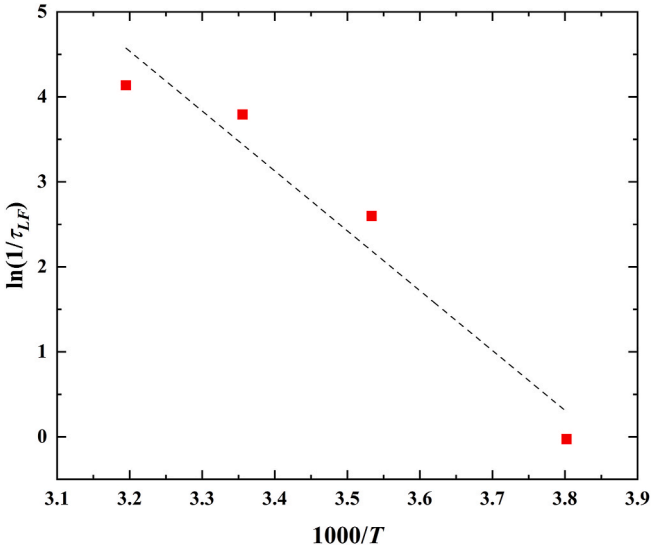

Fig. 10. Arrhenius plot $\ln(1/\tau_{LF})$ versus $1000/T$. The symbols are the experimental data, and the solid line is the least-square fit.

(mediated by vacancy defects) is responsible of the *J-V* curve hysteresis, with no significant long-rate transport of Pb^{2+} or MA^{+} cations. According to literature, the activation energy for I^{-} in the standard $MAPbI_3$ based solar cells is 0.29–0.38 eV [64,71,77,78]. Comparing these results with those obtained for CsRbFAMA solar cells, the quadruple-cation perovskite is characterized by larger iodide ion activation energy which results into a lower ionic conductivity that has a positive effect on device stability. The cations size mismatch of the mixed "A" leads to a steric effect that hampers the migration pathways of iodide ions, increasing the activation energy, and reducing iodide ion migration [74,79]. The origin of the performance improvements has been identified as several factors. On one hand, the addition of smaller inorganic cations produces a contraction of the unit cell volume whose origin is associated with the tilting of the PbI_6 octahedra in the structure. Furthermore, the oscillation of this octahedra is reduced resulting in a "locked" PbI_6 octahedral framework. On the other hand, the organic FA^{+} or MA^{+} molecular ions in A-site undergo rotational motion inside the inorganic PbI_6 octahedral cage. The incorporation of smaller cations reduces this oscillation and, therefore, the lattice dynamics, which may confer greater structural stability [74]. Consequently, the mixed composition devices exhibit significantly improved thermal stability. To our knowledge, this is the first time that iodide ion activation energy has been calculated in CsRbFAMA based devices, quantifying iodide ion migration, and explaining the more stable lattice configuration.

A higher E_{ion} leads to a lower diffusion coefficient (D), according to the equation:

$$D = \frac{v_0 d^2}{6} e^{-\frac{E_{ion}}{k_B T}} \tag{6}$$

where v_0 is the attempt-to escape frequency of an ionic jump and d is the jump distance [80]. The attempt frequency is assumed to be in the order of 10^{12} s^{-1} [81] and a jump distance of 4.49 Å was used [82]. At 300 K, we obtain a diffusion coefficient of the order of $D = 10^{-14}$ cm^2 s^{-1} for iodine ions in CsRbFAMA, which is five orders of magnitude lower that the diffusion coefficient $D = 10^{-9}$ cm^2 s^{-1} previously reported for iodine ions in $MAPbI_3$ [77,78].

In view of the results, we can corroborate that CsRbFAMA based solar cells present a higher stability than $MAPbI_3$ due to a reduction of the halide ion migration, even at high temperatures.

On the other hand, temperature measurements of *IS* in dark for CsRbMAFA based solar cells have been carried out. The chosen frequency regime ensures that the measured capacitance is not affected by capacitance attributed to ion diffusion through the transport layers (Fig. 11.a). At low frequencies, results show a constant plateau where the capacitance is dominated by the depletion capacitance. At very high frequencies, the capacitance is limited by the series resistance of the device.

We have carried out a Mott-Schottky analysis using the capacitance at 10 kHz, at the plateau of the capacitance in Fig. 11.a, to ensure that the capacitance corresponds to the geometric capacitance and the effect of series resistance can be neglected. Fig. 11.b shows C^{-2} as a function of voltage, and it reveals a plateau at low voltages, indicating a full depletion under low applied bias. Although the curves follow the same trend for all temperatures, we have selected 263 K to minimize any ionic capacitance contribution. In the case of full depletion, the geometrical capacitance can be related to the perovskite permittivity (ε) by $C_{geo} = \varepsilon\varepsilon_0 A/t$, where ε_0 is the vacuum permittivity, t is the thickness of the active layer and A is the area of the active layer. The obtained ε is 32.7 for the perovskite layer permittivity in agreement with literature [83–85].

In dark conditions at low forward bias, the depletion capacitance as a function of applied voltage can be approximated by the Mott-Schottky relation as:

$$C_{dl} = \sqrt{\frac{q\varepsilon_0 \varepsilon N_A}{2(V_{bi} - V)}} \tag{7}$$

where q is the elementary charge, N_A the doping density, and V_{bi} the built-in potential. From the C^{-2} vs. V plot (Fig. 11.b) we have obtained a $V_{bi} = 0.86$ V and a doping density $N_A = 7.27{\cdot}10^{15}$ cm^{-3}. This value of N_A is significantly lower than $N_A = 10^{17}$ cm^{-3} reported for $MAPbI_3$ [86]. Previous theoretical calculations predict that the p-type doping of $MAPbI_3$ originates from negatively charged Pb^{2+} and MA^{+} vacancies while positively charged I^{-} vacancies may result in n-type doping [87]. In our devices, the low value of N_A leads us to conclude that CsRbFAMA based solar cells present a more stable cation structure, at least at room temperature or below. It is worth mentioning that although it would be desirable to estimate N_A at high temperatures, the Mott-Schottky analysis is only meaningful when the depletion capacitance can be clearly identified, and at high temperatures the capacitance attributed to ion migration may not be neglected.

3.1. Numerical simulations

To obtain further validation of our hypotheses, we have performed 2D numerical simulations employing the software SILVACO TCAD ATLAS and using the layer structure FTO/TiO_x/perovskite/spiro-OMeTAD/Au. Electrical and optical parameters for all layers are shown in Table S1 of Supplementary Information and in the literature [88–91]. Layer doping and thicknesses correspond to experimental data.

First, *J-V* curves have been simulated under different illuminations levels using AM1.5G spectrum, with intensities from 0.01 to 1-sun. Device temperature has been varied from 240 to 360 K. Ideality factor as a function of device temperature has been calculated from the dependence of V_{OC} with light intensity, as depicted previously. Simulations include the three main minority carrier recombination pathways: radiative (band-to-band) processes, SRH recombination in the bulk, and

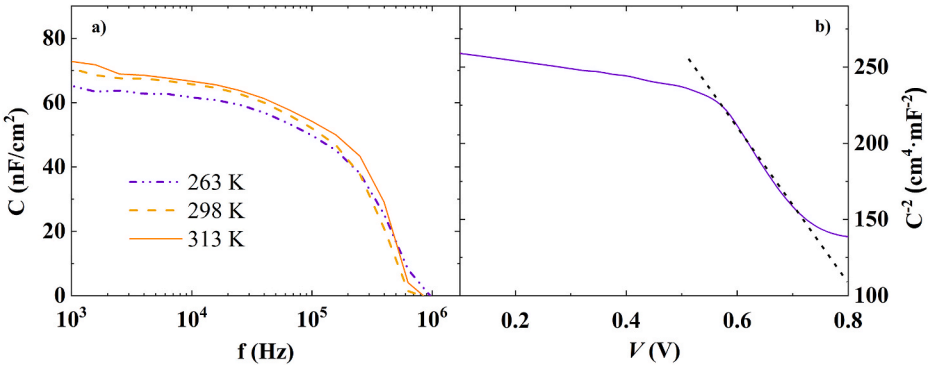

Fig. 11. a) Impedance spectroscopy measured in the dark at 0 V with an AC perturbation of 20 mV. b) Mott-Schottky characteristics measured at 263 K with an AC perturbation of 20 mV at 10 kHz.

interfacial recombination at the perovskite/HTL interface. To reproduce more accurately the experimental device parameters, a bulk SRH minority carrier lifetime of 10^{-6} s has been used. Regarding the surface recombination velocities (SRV) in the perovskite/HTL interface, a value of 10^6 cm/s has been selected.

Fig. 12 shows that the simulated ideality factor decreases steadily with device temperature from 1.5 to 1.3 in the 240–300 K temperature range, while from 300 K to 360 K the decrease is smoothed out and the η values remain practically constant. These results reproduce fairly close the experimental trends already shown in Fig. 6, and corroborate that for low temperature, these devices are dominated by SRH recombination in the bulk, while for higher temperatures the interfacial recombination at the perovskite/spiro OMeTAD takes the leading role. In addition, radiative recombination is negligible in all the temperature range in this kind of devices.

Furthermore, V_{OC} slope with temperature has been calculated from simulated data. The extracted value of −1.48 mV/K (also shown in Fig. 12) is quite close to the experimental value −1.63 mV/K. It is worth mentioning that to model the perovskite active layer, a temperature-dependent bandgap has been used, based on the universal energy bandgap model (equation (8)), fitted to reproduce experimental values. The model parameters are $E_{g300} = 1.609\,eV$, $E_{G\alpha} = -4.73{\cdot}10^{-4}\,eV/K$ and $E_{g\beta} = 0\,K$.

$$E_g = E_{g300} + E_{G\alpha}\left(\frac{300^2}{300 + E_{G\beta}} - \frac{T^2}{T + E_{g\beta}}\right) \tag{8}$$

Besides, in order to demonstrate the strong dependence of FF on the HTL electrical conductivity, we have performed a different set of numerical simulations at room temperature and 1-sun illumination, varying the spiro-OMeTAD carrier mobility, from $1{\cdot}10^{-6}$ up to $1{\cdot}10^{-3}$ $cm^2/(V{\cdot}s)$. Fig. 13 shows that a small variation in this parameter can significantly affect the overall device performance. In particular, in our simulations, increasing the mobility from $1{\cdot}10^{-6}$ up to $1{\cdot}10^{-5}$ $cm^2/V{\cdot}s$, it results in an improvement of the FF from 0.67 to 0.81, while J_{SC} and V_{OC} remain unchanged. A further increase in mobility does not imply a significant increase in FF. Thus, our experimental reduction of about 10% in FF can easily be correlated with a decrease of the spiro-OMeTAD mobility of less than one order of magnitude.

4. Conclusions

In this work, we have studied recombination mechanisms and ion migration in mixed-cation mixed-halide PSC based on $Cs_{0.05}Rb_{0.05}(FA_{0.83}MA_{0.17})_{0.9}Pb(I_{0.83}Br_{0.17})_3$ by means of the temperature dependence of the *J-V* and *IS* measurements in the range of 253 K up to 333 K. It is shown that for low temperatures (from 253 up to 323 K), SRH recombination governs, while for temperatures above 323 K surface recombination is the dominant recombination mechanism due to the presence of non-selective contacts, leading to a worsening of device performance. This worsening is attributed to the degradation of the interface perovskite/spiro-OMeTAD and to the decrease of the conduction of the spiro-OMeTAD used as hole transport layer.

On the other hand, our devices show an increased ionic activation energy (0.63 ± 0.08 eV), a lower diffusion coefficient (of the order of 10^{-14} $cm^2\,s^{-1}$) and a lower defect density in the active layer ($7.27{\cdot}10^{15}$ cm^{-3}) compared to conventional methylammonium lead iodide devices. To our knowledge, this is the first time that these parameters have been estimated in CsRbFAMA based solar cells. The incorporation of smaller cations reduces the oscillation dynamics of the structure and, therefore, the lattice dynamics, conferring greater structural stability. Consequently, the mixed composition devices exhibit significantly improved thermal stability.

Therefore, we can conclude that worsening in performance of these devices at high temperature is not attributed to the degradation of the perovskite layer CsRbFAMA itself, but it is mainly due to the modification of the spiro-OMeTAD conduction ability and the deterioration of the perovskite/spiro-OMeTAD interface.

Finally, 2D numerical simulations performed with SILVACO ATLAS TCAD corroborate the strong influence of the spiro-OMeTAD conductivity degradation in the device FF. Moreover, simulations have shown that SRH recombination in the bulk is the dominating mechanism at low temperature while as the temperature raises the ideality factor decreases suggesting that SRH recombination is governed by the interface.

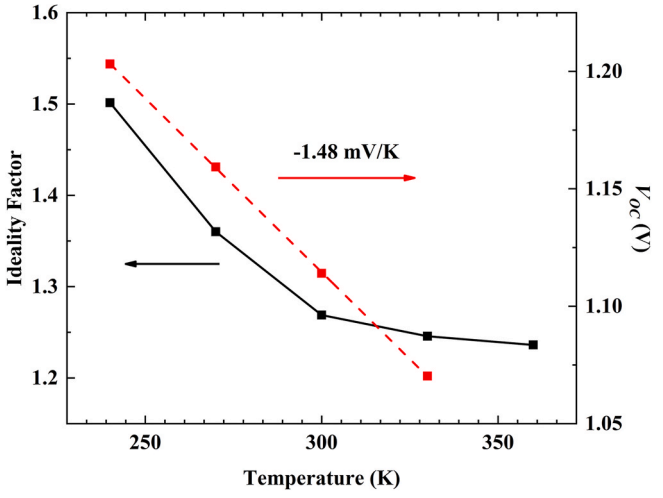

Fig. 12. Evolution of open circuit voltage (dash line) and ideality factor (straight line) with temperature, obtained from numerical simulations with SILVACO TCAD ATLAS.

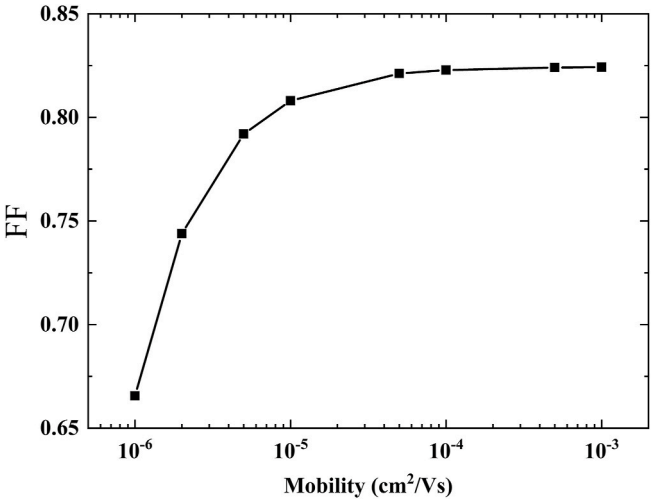

Fig. 13. Fill factor obtained from simulated devices at room temperature and 1-sun illumination, with different spiro-OMeTAD mobilities.

Author contributions

All authors contributed to the manuscript and were involved in the discussion of results. Device manufacture, **M.C.L.-G.**; characterization, **M.C.L.-G., S.D., M.G.-P.**; circuital modeling, **M.C.L.-G. and S.D.**; data processing, **M.C.L.-G., S.D. and G.d.P.**; physical modelling and numerical simulations, **G.d.P. and D.M.-M.**; writing-review and editing, **B.A., B.R. G.d.P., D.M.-M. and M.C.L.-G.**; funding acquisition, **B.A., and B.R.** All authors have read and agreed to the published version of the manuscript.

Declaration of competing interest

The authors declare that they have no known competing financial interests or personal relationships that could have appeared to influence the work reported in this paper.

Data availability

Data will be made available on request.

Acknowledgements

This research was funded by Community of Madrid under the SINFOTON2-CM Research Program (S2018/NMT-4326-SINFOTON2-CM), and in the framework of the Multiannual Agreement with the Rey Juan Carlos University in line of action 1, "Encouragement of Young Phd students investigation" (Ref. M2180, "SolGenALEE"), and by Universidad Rey Juan Carlos with Research Projects M2607, M2180 and M2363. M.G.P. acknowledges the MCIN/AEI for the financial support provide for the project ALPHOMENA_PID2021-123190OB-I00 (LAser assembled Integrable PHOtonic MEtasurfaces & NAnostructures). M.C. L.-G. particularly expresses her gratitude to Lidia Contreras Bernal from ICMS (CSIC-Universidad de Sevilla) for their valuable help in perovskite solar cells fabrication.

Appendix A. Supplementary data

Supplementary data to this article can be found online at https://doi.org/10.1016/j.orgel.2023.106843.

References

[1] A. Kojima, K. Teshima, Y. Shirai, T. Miyasaka, Organometal halide perovskites as visible-light sensitizers for photovoltaic cells, J. Am. Chem. Soc. 131 (2009) 6050–6051, https://doi.org/10.1021/ja809598r.
[2] L. Lin, N.M. Ravindra, Temperature dependence of CIGS and perovskite solar cell performance: an overview, SN Appl. Sci. 2 (2020) 1361, https://doi.org/10.1007/s42452-020-3169-2.
[3] Best research-cell efficiency chart – national renewable energy laboratory. https://www.nrel.gov/pv/assets/pdfs/best-research-cell-efficiencies.pdf, 2023.
[4] H.S. Jung, N.-G. Park, Perovskite solar cells: from materials to devices, Small 11 (2015) 10–25, https://doi.org/10.1002/smll.201402767.
[5] S. De Wolf, J. Holovsky, S.-J. Moon, P. Löper, B. Niesen, M. Ledinsky, F.-J. Haug, J.-H. Yum, C. Ballif, Organometallic halide perovskites: sharp optical absorption edge and its relation to photovoltaic performance, J. Phys. Chem. Lett. 5 (2014) 1035–1039, https://doi.org/10.1021/jz500279b.
[6] C. Wehrenfennig, G.E. Eperon, M.B. Johnston, H.J. Snaith, L.M. Herz, High charge carrier mobilities and lifetimes in organolead trihalide perovskites, Adv. Mater. 26 (2014) 1584–1589, https://doi.org/10.1002/adma.201305172.
[7] S.D. Stranks, G.E. Eperon, G. Grancini, C. Menelaou, M.J.P. Alcocer, T. Leijtens, L. M. Herz, A. Petrozza, H.J. Snaith, Electron-hole diffusion lengths exceeding 1 micrometer in an organometal trihalide perovskite absorber, Science 342 (2013) 341–344, https://doi.org/10.1126/science.1243982.
[8] W.-J. Yin, T. Shi, Y. Yan, Unusual defect physics in $CH_3NH_3PbI_3$ perovskite solar cell absorber, Appl. Phys. Lett. 104 (2014), 063903, https://doi.org/10.1063/1.4864778.
[9] J. Kim, S.-H. Lee, J.H. Lee, K.-H. Hong, The role of intrinsic defects in methylammonium lead iodide perovskite, J. Phys. Chem. Lett. 5 (2014) 1312–1317, https://doi.org/10.1021/jz500370k.
[10] F. Di Giacomo, A. Fakharuddin, R. Jose, T.M. Brown, Progress, challenges and perspectives in flexible perovskite solar cells, Energy Environ. Sci. 9 (2016) 3007–3035, https://doi.org/10.1039/C6EE01137C.
[11] T.A. Berhe, W.-N. Su, C.-H. Chen, C.-J. Pan, J.-H. Cheng, H.-M. Chen, M.-C. Tsai, L.-Y. Chen, A.A. Dubale, B.-J. Hwang, Organometal halide perovskite solar cells: degradation and stability, Energy Environ. Sci. 9 (2016) 323–356, https://doi.org/10.1039/C5EE02733K.
[12] M.I. Asghar, J. Zhang, H. Wang, P.D. Lund, Device stability of perovskite solar cells – a review, Renew. Sustain. Energy Rev. 77 (2017) 131–146, https://doi.org/10.1016/j.rser.2017.04.003.
[13] R. Wang, M. Mujahid, Y. Duan, Z.-K. Wang, J. Xue, Y. Yang, A review of perovskites solar cell stability, Adv. Funct. Mater. (2019), https://doi.org/10.1002/adfm.201808843.
[14] K.J. Xu, R.T. Wang, A.F. Xu, J.Y. Chen, G. Xu, Hysteresis and instability predicted in moisture degradation of perovskite solar cells, ACS Appl. Mater. Interfaces 12 (2020) 48882–48889, https://doi.org/10.1021/acsami.0c17323.
[15] N. Aristidou, I. Sanchez-Molina, T. Chotchuangchutchaval, M. Brown, L. Martinez, T. Rath, S.A. Haque, The role of oxygen in the degradation of methylammonium lead trihalide perovskite photoactive layers, Angew. Chem. Int. Ed. 54 (2015) 8208–8212, https://doi.org/10.1002/anie.201503153.
[16] N. Aristidou, C. Eames, I. Sanchez-Molina, X. Bu, J. Kosco, M.S. Islam, S.A. Haque, Fast oxygen diffusion and iodide defects mediate oxygen-induced degradation of perovskite solar cells, Nat. Commun. 8 (2017), 15218, https://doi.org/10.1038/ncomms15218.
[17] D. Bryant, N. Aristidou, S. Pont, I. Sanchez-Molina, T. Chotchunangatchaval, S. Wheeler, J.R. Durrant, S.A. Haque, Light and oxygen induced degradation limits the operational stability of methylammonium lead triiodide perovskite solar cells, Energy Environ. Sci. 9 (2016) 1655–1660, https://doi.org/10.1039/C6EE00409A.
[18] S.-W. Lee, S. Kim, S. Bae, K. Cho, T. Chung, L.E. Mundt, S. Lee, S. Park, H. Park, M. C. Schubert, S.W. Glunz, Y. Ko, Y. Jun, Y. Kang, H.-S. Lee, D. Kim, UV degradation and recovery of perovskite solar cells, Sci. Rep. 6 (2016), 38150, https://doi.org/10.1038/srep38150.
[19] A. Farooq, I.M. Hossain, S. Moghadamzadeh, J.A. Schwenzer, T. Abzieher, B. S. Richards, E. Klampaftis, U.W. Paetzold, Spectral dependence of degradation under ultraviolet light in perovskite solar cells, ACS Appl. Mater. Interfaces 10 (2018) 21985–21990, https://doi.org/10.1021/acsami.8b03024.
[20] Y. Li, X. Xu, C. Wang, B. Ecker, J. Yang, J. Huang, Y. Gao, Light-induced degradation of $CH_3NH_3PbI_3$ hybrid perovskite thin film, J. Phys. Chem. C 121 (2017) 3904–3910, https://doi.org/10.1021/acs.jpcc.6b11853.
[21] N. Papež, A. Gajdoš, R. Dallaev, D. Sobola, P. Sedlák, R. Motúz, A. Nebojsa, L. Grmela, Performance analysis of GaAs based solar cells under gamma irradiation, Appl. Surf. Sci. 510 (2020), 145329, https://doi.org/10.1016/j.apsusc.2020.145329.
[22] R.K. Misra, S. Aharon, B. Li, D. Mogilyansky, I. Visoly-Fisher, L. Etgar, E.A. Katz, Temperature- and component-dependent degradation of perovskite photovoltaic materials under concentrated sunlight, J. Phys. Chem. Lett. 6 (2015) 326–330, https://doi.org/10.1021/jz502642b.
[23] G. Abdelmageed, C. Mackeen, K. Hellier, L. Jewell, L. Seymour, M. Tingwald, F. Bridges, J.Z. Zhang, S. Carter, Effect of temperature on light induced degradation in methylammonium lead iodide perovskite thin films and solar cells, Sol. Energy Mater. Sol. Cells 174 (2018) 566–571, https://doi.org/10.1016/j.solmat.2017.09.053.
[24] E.J. Juarez-Perez, Z. Hawash, S.R. Raga, L.K. Ono, Y. Qi, Thermal degradation of $CH_3NH_3PbI_3$ perovskite into NH_3 and CH_3I gases observed by coupled thermogravimetry–mass spectrometry analysis, Energy Environ. Sci. 9 (2016) 3406–3410, https://doi.org/10.1039/C6EE02016J.
[25] Y.A. Olanrewaju, K. Orisekeh, O.V. Oyelade, R.K. Koech, R. Ichwani, A.I. Ebunu, D. I. Amune, A. Bello, V.C. Anye, O.K. Oyewole, W.O. Soboyejo, Effects of temperature-dependent burn-in decay on the performance of triple cation mixed halide perovskite solar cells, AIP Adv. 12 (2022), 015122, https://doi.org/10.1063/5.0078821.
[26] T.J. Jacobsson, W. Tress, J.-P. Correa-Baena, T. Edvinsson, A. Hagfeldt, Room temperature as a goldilocks environment for CH3NH3PbI3 perovskite solar cells: the importance of temperature on device performance, J. Phys. Chem. C (2016) 12.
[27] T. Moot, J.B. Patel, G. McAndrews, E.J. Wolf, D. Morales, I.E. Gould, B.A. Rosales, C.C. Boyd, L.M. Wheeler, P.A. Parilla, S.W. Johnston, L.T. Schelhas, M.D. McGehee, J.M. Luther, Temperature coefficients of perovskite photovoltaics for energy yield calculations, ACS Energy Lett. 6 (2021) 2038–2047, https://doi.org/10.1021/acsenergylett.1c00748.
[28] Q. Zhou, B. Wang, R. Meng, J. Zhou, S. Xie, X. Zhang, J. Wang, S. Yue, B. Qin, H. Zhou, Y. Zhang, Understanding temperature-dependent charge extraction and trapping in perovskite solar cells, Adv. Funct. Mater. 30 (2020), 2000550, https://doi.org/10.1002/adfm.202000550.
[29] Y. Rong, Y. Hu, A. Mei, H. Tan, M.I. Saidaminov, S.I. Seok, M.D. McGehee, E. H. Sargent, H. Han, Challenges for commercializing perovskite solar cells, Science 361 (2018), eaat8235, https://doi.org/10.1126/science.aat8235.
[30] S. Shao, J. Liu, H.-H. Fang, L. Qiu, G.H. ten Brink, J.C. Hummelen, L.J.A. Koster, M. A. Loi, Efficient perovskite solar cells over a broad temperature window: the role of the charge carrier extraction, Adv. Energy Mater. 7 (2017), 1701305, https://doi.org/10.1002/aenm.201701305.
[31] I. Mesquita, L. Andrade, A. Mendes, Temperature impact on perovskite solar cells under operation, ChemSusChem 12 (2019) 2186–2194, https://doi.org/10.1002/cssc.201802899.
[32] M.A. Green, A. Ho-Baillie, H.J. Snaith, The emergence of perovskite solar cells, Nat. Photonics 8 (2014) 506–514, https://doi.org/10.1038/nphoton.2014.134.
[33] S. Tan, I. Yavuz, N. De Marco, T. Huang, S. Lee, C.S. Choi, M. Wang, S. Nuryyeva, R. Wang, Y. Zhao, H. Wang, T. Han, B. Dunn, Y. Huang, J. Lee, Y. Yang, Steric impediment of ion migration contributes to improved operational stability of perovskite solar cells, Adv. Mater. 32 (2020), 1906995, https://doi.org/10.1002/adma.201906995.
[34] B. Philippe, M. Saliba, J.-P. Correa-Baena, U.B. Cappel, S.-H. Turren-Cruz, M. Grätzel, A. Hagfeldt, H. Rensmo, Chemical distribution of multiple cation (Rb^+, Cs^+, MA^+, and FA^+) perovskite materials by photoelectron spectroscopy, Chem. Mater. 29 (2017) 3589–3596, https://doi.org/10.1021/acs.chemmater.7b00126.
[35] J.-P. Correa-Baena, A. Abate, M. Saliba, W. Tress, T.J. Jacobsson, M. Grätzel, A. Hagfeldt, The rapid evolution of highly efficient perovskite solar cells, Energy Environ. Sci. 10 (2017) 710–727, https://doi.org/10.1039/C6EE03397K.
[36] X. Zhao, N.-G. Park, Stability issues on perovskite solar cells, Photonics 2 (2015) 1139–1151, https://doi.org/10.3390/photonics2041139.
[37] G.P. Nagabhushana, R. Shivaramaiah, A. Navrotsky, Direct calorimetric verification of thermodynamic instability of lead halide hybrid perovskites, Proc.

Natl. Acad. Sci. USA 113 (2016) 7717–7721, https://doi.org/10.1073/pnas.1607850113.
[38] E.J. Juarez-Perez, L.K. Ono, Y. Qi, Thermal degradation of formamidinium based lead halide perovskites into sym-triazine and hydrogen cyanide observed by coupled thermogravimetry - mass spectrometry analysis, J. Mater. Chem. A. 7 (2019) 16912–16919, https://doi.org/10.1039/C9TA06058H.
[39] A. Binek, F.C. Hanusch, P. Docampo, T. Bein, Stabilization of the trigonal high-temperature phase of formamidinium lead iodide, J. Phys. Chem. Lett. 6 (2015) 1249–1253, https://doi.org/10.1021/acs.jpclett.5b00380.
[40] T. Matsui, T. Yamamoto, T. Nishihara, R. Morisawa, T. Yokoyama, T. Sekiguchi, T. Negami, Compositional engineering for thermally stable, highly efficient perovskite solar cells exceeding 20% power conversion efficiency with 85 °C/85% 1000 h stability, Adv. Mater. 31 (2019), 1806823, https://doi.org/10.1002/adma.201806823.
[41] M. Saliba, T. Matsui, K. Domanski, J.-Y. Seo, A. Ummadisingu, M. Zakeeruddin, J.-P. Correa-Baena, W.R. Tress, A. Abate, A. Hagfeldt, M. Grätzel, Incorporation of Rubidium Cations into Perovskite Solar Cells Improves Photovoltaic Performance, 2016, p. 9.
[42] B. Gao, J. Meng, RbCs(MAFA)PbI3 perovskite solar cell with 22.81% efficiency using the precise ions cascade regulation, Appl. Surf. Sci. 530 (2020), 147240, https://doi.org/10.1016/j.apsusc.2020.147240.
[43] M. Saliba, T. Matsui, J.-Y. Seo, K. Domanski, J.-P. Correa-Baena, M.K. Nazeeruddin, S.M. Zakeeruddin, W. Tress, A. Abate, A. Hagfeldt, M. Grätzel, Cesium-containing triple cation perovskite solar cells: improved stability, reproducibility and high efficiency, Energy Environ. Sci. 9 (2016) 1989–1997, https://doi.org/10.1039/C5EE03874J.
[44] P. Yadav, M.I. Dar, N. Arora, E.A. Alharbi, F. Giordano, S.M. Zakeeruddin, M. Grätzel, The role of rubidium in multiple-cation-based high-efficiency perovskite solar cells, Adv. Mater. 29 (2017), 1701077, https://doi.org/10.1002/adma.201701077.
[45] Y. Hu, E.M. Hutter, P. Rieder, I. Grill, J. Hanisch, M.F. Aygüler, A.G. Hufnagel, M. Handloser, T. Bein, A. Hartschuh, K. Tvingstedt, V. Dyakonov, A. Baumann, T. J. Savenije, M.L. Petrus, P. Docampo, Understanding the role of cesium and rubidium additives in perovskite solar cells: trap states, charge transport, and recombination, Adv. Energy Mater. 8 (2018), 1703057, https://doi.org/10.1002/aenm.201703057.
[46] J.P. Bastos, G. Uytterhoeven, W. Qiu, U.W. Paetzold, D. Cheyns, S. Surana, J. Rivas, M. Jaysankar, W. Song, T. Aernouts, J. Poortmans, R. Gehlhaar, Model for the prediction of the lifetime and energy yield of methyl ammonium lead iodide perovskite solar cells at elevated temperatures, ACS Appl. Mater. Interfaces 11 (2019) 16517–16526, https://doi.org/10.1021/acsami.9b00923.
[47] G. Divitini, S. Cacovich, F. Matteocci, L. Cinà, A. Di Carlo, C. Ducati, In situ observation of heat-induced degradation of perovskite solar cells, Nat. Energy 1 (2016), 15012, https://doi.org/10.1038/nenergy.2015.12.
[48] Z. Hawash, L.K. Ono, Y. Qi, Recent advances in spiro-MeOTAD hole transport material and its applications in organic–inorganic halide perovskite solar cells, Adv. Mater. Interfac. 5 (2018), 1700623, https://doi.org/10.1002/admi.201700623.
[49] A.K. Jena, Y. Numata, M. Ikegami, T. Miyasaka, Role of spiro-OMeTAD in performance deterioration of perovskite solar cells at high temperature and reuse of the perovskite films to avoid Pb-waste, J. Mater. Chem. A. 6 (2018) 2219–2230, https://doi.org/10.1039/C7TA07674F.
[50] K. Domanski, J.-P. Correa-Baena, N. Mine, M.K. Nazeeruddin, A. Abate, M. Saliba, W. Tress, A. Hagfeldt, M. Grätzel, Not all that glitters is gold: metal-migration-induced degradation in perovskite solar cells, ACS Nano 10 (2016) 6306–6314, https://doi.org/10.1021/acsnano.6b02613.
[51] C.R. Osterwald, T. Glatfelter, Burdick, E.C. Devices, 1987_Comparison of the Temperature Coefficients of the Basic IV Parameters for Various Types of Solar Cells, 1987, pp. 188–193.
[52] O. Dupré, R. Vaillon, M.A. Green, Physics of the temperature coefficients of solar cells, Sol. Energy Mater. Sol. Cells 140 (2015) 92–100, https://doi.org/10.1016/j.solmat.2015.03.025.
[53] M.A. Green, General temperature dependence of solar cell performance and implications for device modelling, Prog. Photovoltaics Res. Appl. 11 (2003) 333–340, https://doi.org/10.1002/pip.496.
[54] W. Tress, M. Yavari, K. Domanski, P. Yadav, B. Niesen, J.P.C. Baena, A. Hagfeldt, M. Graetzel, Interpretation and evolution of open-circuit voltage, recombination, ideality factor and subgap defect states during reversible light-soaking and irreversible degradation of perovskite solar cells, Energy Environ. Sci. 11 (2018) 151–165, https://doi.org/10.1039/C7EE02415K.
[55] J.A. Schwenzer, L. Rakocevic, R. Gehlhaar, T. Abzieher, S. Gharibzadeh, S. Moghadamzadeh, A. Quintilla, B.S. Richards, U. Lemmer, U.W. Paetzold, Temperature variation-induced performance decline of perovskite solar cells, ACS Appl. Mater. Interfaces 10 (2018) 16390–16399, https://doi.org/10.1021/acsami.8b01033.
[56] M.A. Green, Radiative efficiency of state-of-the-art photovoltaic cells: radiative efficiency of photovoltaic cells, Prog. Photovoltaics Res. Appl. 20 (2012) 472–476, https://doi.org/10.1002/pip.1147.
[57] W.L. Leong, Z.-E. Ooi, D. Sabba, C. Yi, S.M. Zakeeruddin, M. Graetzel, J.M. Gordon, E.A. Katz, N. Mathews, Identifying fundamental limitations in halide perovskite solar cells, Adv. Mater. 28 (2016) 2439–2445, https://doi.org/10.1002/adma.201505480.
[58] S. Kim, S. Bae, S.-W. Lee, K. Cho, K.D. Lee, H. Kim, S. Park, G. Kwon, S.-W. Ahn, H.-M. Lee, Y. Kang, H.-S. Lee, D. Kim, Relationship between ion migration and interfacial degradation of CH3NH3PbI3 perovskite solar cells under thermal conditions, Sci. Rep. 7 (2017) 1200, https://doi.org/10.1038/s41598-017-00866-6.
[59] A. Dualeh, T. Moehl, N. Tétreault, J. Teuscher, P. Gao, M.K. Nazeeruddin, M. Grätzel, Impedance spectroscopic analysis of lead iodide perovskite-sensitized solid-state solar cells, ACS Nano 8 (2014) 362–373, https://doi.org/10.1021/nn404323g.
[60] A.R. Pascoe, N.W. Duffy, A.D. Scully, F. Huang, Y.-B. Cheng, Insights into planar $CH_3NH_3PbI_3$ perovskite solar cells using impedance spectroscopy, J. Phys. Chem. C 119 (2015) 4444–4453, https://doi.org/10.1021/jp509896u.
[61] B. Romero, G. del Pozo, B. Arredondo Conchillo, D. Martín-Martín, E. Hernández-Balaguera, M. del C. López-González, Characterization of organic and perovskite solar cells by impedance spectroscopy, in: M. Lira-Cantu, Z.H. Kafafi (Eds.), Women Renew. Energy WiRE, SPIE, 2019, p. 22, https://doi.org/10.1117/12.2530568. San Diego, United States.
[62] E. von Hauff, Impedance spectroscopy for emerging photovoltaics, J. Phys. Chem. C 123 (2019) 11329–11346, https://doi.org/10.1021/acs.jpcc.9b00892.
[63] A. Bou, A. Pockett, D. Raptis, T. Watson, M.J. Carnie, J. Bisquert, Beyond impedance spectroscopy of perovskite solar cells: insights from the spectral correlation of the electrooptical frequency techniques, J. Phys. Chem. Lett. 11 (2020) 8654–8659, https://doi.org/10.1021/acs.jpclett.0c02459.
[64] L. Contreras, S. Ramos-Terrón, A. Riquelme, P.P. Boix, J.A. Idígoras, I.M. Seró, J. A. Anta, Impedance analysis of perovskite solar cells: a case study, J. Mater. Chem. (2019), https://doi.org/10.1039/C9TA02808K.
[65] A. Todinova, L. Contreras-Bernal, M. Salado, S. Ahmad, N. Morillo, J. Idígoras, J. A. Anta, Towards a universal approach for the analysis of impedance spectra of perovskite solar cells: equivalent circuits and empirical analysis, Chemelectrochem 4 (2017) 2891–2901, https://doi.org/10.1002/celc.201700498.
[66] I. Zarazua, J. Bisquert, G. Garcia-Belmonte, Light-induced space-charge accumulation zone as photovoltaic mechanism in perovskite solar cells, J. Phys. Chem. Lett. 7 (2016) 525–528, https://doi.org/10.1021/acs.jpclett.5b02810.
[67] E. Hernández-Balaguera, B. Arredondo, G. del Pozo, B. Romero, Exploring the impact of fractional-order capacitive behavior on the hysteresis effects of perovskite solar cells: a theoretical perspective, Commun. Nonlinear Sci. Numer. Simul. 90 (2020), 105371, https://doi.org/10.1016/j.cnsns.2020.105371.
[68] A. Guerrero, G. Garcia-Belmonte, I. Mora-Sero, J. Bisquert, Y.S. Kang, T. J. Jacobsson, J.-P. Correa-Baena, A. Hagfeldt, Properties of contact and bulk impedances in hybrid lead halide perovskite solar cells including inductive loop elements, J. Phys. Chem. C 120 (2016) 8023–8032, https://doi.org/10.1021/acs.jpcc.6b01728.
[69] B. Hailegnaw, N.S. Sariciftci, M.C. Scharber, Impedance spectroscopy of perovskite solar cells: studying the dynamics of charge carriers before and after continuous operation, Phys. Status Solidi A 217 (2020), 2000291, https://doi.org/10.1002/pssa.202000291.
[70] I. Zarazua, G. Han, P.P. Boix, S. Mhaisalkar, F. Fabregat-Santiago, I. Mora-Seró, J. Bisquert, G. Garcia-Belmonte, Surface recombination and collection efficiency in perovskite solar cells from impedance analysis, J. Phys. Chem. Lett. 7 (2016) 5105–5113, https://doi.org/10.1021/acs.jpclett.6b02193.
[71] M. Leoncini, R. Giannuzzi, A. Giuri, S. Colella, A. Listorti, V. Maiorano, A. Rizzo, G. Gigli, S. Gambino, Electronic transport, ionic activation energy and trapping phenomena in a polymer-hybrid halide perovskite composite, J. Sci. Adv. Mater. Devices. 6 (2021) 543–550, https://doi.org/10.1016/j.jsamd.2021.07.006.
[72] J.M. Azpiroz, E. Mosconi, J. Bisquert, F. De Angelis, Defect migration in methylammonium lead iodide and its role in perovskite solar cell operation, Energy Environ. Sci. 8 (2015) 2118–2127, https://doi.org/10.1039/C5EE01265A.
[73] C. Eames, J.M. Frost, P.R.F. Barnes, B.C. O'Regan, A. Walsh, M.S. Islam, Ionic transport in hybrid lead iodide perovskite solar cells, Nat. Commun. 6 (2015) 7497, https://doi.org/10.1038/ncomms8497.
[74] D. Ghosh, P. Walsh Atkins, M.S. Islam, A.B. Walker, C. Eames, Good vibrations: locking of octahedral tilting in mixed-cation iodide perovskites for solar cells, ACS Energy Lett. 2 (2017) 2424–2429, https://doi.org/10.1021/acsenergylett.7b00729.
[75] A. Senocrate, I. Moudrakovski, G.Y. Kim, T.-Y. Yang, G. Gregori, M. Grätzel, J. Maier, The nature of ion conduction in methylammonium lead iodide: a multimethod approach, Angew. Chem. 129 (2017) 7863–7867, https://doi.org/10.1002/ange.201701724.
[76] T.-Y. Yang, G. Gregori, N. Pellet, M. Grätzel, J. Maier, The significance of ion conduction in a hybrid organic-inorganic lead-iodide-based perovskite photosensitizer, Angew. Chem. Int. Ed. 54 (2015) 7905–7910, https://doi.org/10.1002/anie.201500014.
[77] M.H. Futscher, J.M. Lee, L. McGovern, L.A. Muscarella, T. Wang, M.I. Haider, A. Fakharuddin, L. Schmidt-Mende, B. Ehrler, Quantification of ion migration in $CH_3NH_3PbI_3$ perovskite solar cells by transient capacitance measurements, Mater. Horiz. 6 (2019) 1497–1503, https://doi.org/10.1039/C9MH00445A.
[78] L. McGovern, M.H. Futscher, L.A. Muscarella, B. Ehrler, Understanding the stability of MAPbBr3 versus MAPbI3: suppression of methylammonium migration and reduction of halide migration, J. Phys. Chem. Lett. (2020) 7127–7132,, https://doi.org/10.1021/acs.jpclett.0c01822.
[79] D.W. Ferdani, S.R. Pering, D. Ghosh, P. Kubiak, A.B. Walker, S.E. Lewis, A. L. Johnson, P.J. Baker, M.S. Islam, P.J. Cameron, Partial cation substitution reduces iodide ion transport in lead iodide perovskite solar cells, Energy Environ. Sci. 12 (2019) 2264–2272, https://doi.org/10.1039/C9EE00476A.
[80] D. Meggiolaro, E. Mosconi, F. De Angelis, formation of surface defects dominates ion migration in lead-halide perovskites, ACS Energy Lett. 4 (2019) 779–785, https://doi.org/10.1021/acsenergylett.9b00247.

[81] J. Koettgen, T. Zacherle, S. Grieshammer, M. Martin, Ab initio calculation of the attempt frequency of oxygen diffusion in pure and samarium doped ceria, Phys. Chem. Chem. Phys. 19 (2017) 9957–9973, https://doi.org/10.1039/C6CP04802A.
[82] D.W. Ferdani, A.L. Johnson, S.E. Lewis, P.J. Baker, P.J. Cameron, Opposites attract – muons as direct probes for iodide diffusion in methyl ammonium lead iodide, Mater. Sci. (2018), https://doi.org/10.48550/ARXIV.1801.03845.
[83] Q. Dong, Y. Fang, Y. Shao, P. Mulligan, J. Qiu, L. Cao, J. Huang, Electron-hole diffusion lengths > 175 μm in solution-grown CH $_3$ NH $_3$ PbI $_3$ single crystals, Science 347 (2015) 967–970, https://doi.org/10.1126/science.aaa5760.
[84] F.F. Targhi, Y.S. Jalili, F. Kanjouri, MAPbI3 and FAPbI3 perovskites as solar cells: case study on structural, electrical and optical properties, Results Phys. 10 (2018) 616–627, https://doi.org/10.1016/j.rinp.2018.07.007.
[85] G.-J.A.H. Wetzelaer, M. Scheepers, A.M. Sempere, C. Momblona, J. Ávila, H. J. Bolink, Trap-assisted non-radiative recombination in organic-inorganic perovskite solar cells, Adv. Mater. 27 (2015) 1837–1841, https://doi.org/10.1002/adma.201405372.
[86] O. Almora, C. Aranda, E. Mas-Marzá, G. Garcia-Belmonte, On Mott-Schottky analysis interpretation of capacitance measurements in organometal perovskite solar cells, Appl. Phys. Lett. 109 (2016), 173903, https://doi.org/10.1063/1.4966127.
[87] L.A. Frolova, N.N. Dremova, P.A. Troshin, The chemical origin of the p-type and n-type doping effects in the hybrid methylammonium–lead iodide ($MAPbI_3$) perovskite solar cells, Chem. Commun. 51 (2015) 14917–14920, https://doi.org/10.1039/C5CC05205J.
[88] Y. Guo, Q. Wang, W.A. Saidi, Structural stabilities and electronic properties of high-angle grain boundaries in perovskite cesium lead halides, J. Phys. Chem. C 121 (2017) 1715–1722, https://doi.org/10.1021/acs.jpcc.6b11434.
[89] N.J. Jeon, H.G. Lee, Y.C. Kim, J. Seo, J.H. Noh, J. Lee, S.I. Seok, *o* -methoxy substituents in spiro-OMeTAD for efficient inorganic–organic hybrid perovskite solar cells, J. Am. Chem. Soc. 136 (2014) 7837–7840, https://doi.org/10.1021/ja502824c.
[90] L. Pedesseau, M. Kepenekian, D. Sapori, Y. Huang, A. Rolland, A. Beck, C. Cornet, O. Durand, S. Wang, C. Katan, J. Even, in: A. Freundlich, L. Lombez, M. Sugiyama (Eds.), Dielectric Properties of Hybrid Perovskites and Drift-Diffusion Modeling of Perovskite Cells, 2016, p. 97430N, https://doi.org/10.1117/12.2214007. San Francisco, California, United States.
[91] Y. Zhou, F. Huang, Y.-B. Cheng, A. Gray-Weale, Numerical analysis of a hysteresis model in perovskite solar cells, Comput. Mater. Sci. 126 (2017) 22–28, https://doi.org/10.1016/j.commatsci.2016.09.010.